MITSUBISHI ELECTRIC RESEARCH LABORATORIES
https://www.merl.com

Induction Motor Eccentricity Fault Detection and Quantification using Topological Data Analysis

Wang, Bingnan; Lin, Chungwei; Inoue, Hiroshi; Kanemaru, Makoto

TR2024-063 June 05, 2024

Abstract

In this paper, we propose a topological data analysis (TDA) method for the processing of induction motor stator current data, and apply it to the detection and quantification of eccentricity faults. Traditionally, physics-based models and involved signal processing techniques are required to identify and extract the subtle frequency components in current data related to a particular fault. We show that TDA offers an alternative way to extract fault related features, and effectively distinguish data from different fault conditions. We will introduce TDA method and the procedure of extracting topological features from time-domain data, and apply it to induction motor current data measured under different eccentricity fault conditions. We show that while the raw time-domain data are very challenging to distinguish, the extracted topological features from these data are distinct and highly associated with eccentricity fault level. With TDA processed data, we can effectively train machine learning models to predict fault levels with good accuracy, even for new data from eccentricity levels that are not seen in the training data. The proposed method is model-free, and only requires a small segment of time-domain data to make prediction. These advantages make it attractive for a wide range of data-driven fault detection applications.

IEEE Access 2024

Mitsubishi Electric Research Laboratories, Inc.
201 Broadway, Cambridge, Massachusetts 02139

Induction Motor Eccentricity Fault Detection and Quantification using Topological Data Analysis

Bingnan Wang[1, *], Chungwei Lin[1], Hiroshi Inoue[2] and Makoto Kanemaru[2]

[1]Mitsubishi Electric Research Laboratories (MERL),
201 Broadway, Cambridge, MA 02139 USA
[2]Advanced Technology R&D Center,
Mitsubishi Electric Corporation, Amagasaki, Japan
[*]Email: bwang@merl.com

***Abstract*—In this paper, we propose a topological data analysis (TDA) method for the processing of induction motor stator current data, and apply it to the detection and quantification of eccentricity faults. Traditionally, physics-based models and involved signal processing techniques are required to identify and extract the subtle frequency components in current data related to a particular fault. We show that TDA offers an alternative way to extract fault related features, and effectively distinguish data from different fault conditions. We will introduce TDA method and the procedure of extracting topological features from time-domain data, and apply it to induction motor current data measured under different eccentricity fault conditions. We show that while the raw time-domain data are very challenging to distinguish, the extracted topological features from these data are distinct and highly associated with eccentricity fault level. With TDA processed data, we can effectively train machine learning models to predict fault levels with good accuracy, even for new data from eccentricity levels that are not seen in the training data. The proposed method is model-free, and only requires a small segment of time-domain data to make prediction. These advantages make it attractive for a wide range of data-driven fault detection applications.**

***Index Terms*—Electric Machines, Fault Detection, Machine Learning, Topological Data Analysis**

I. Introduction

ELECTRIC machines, especially motors, are broadly used to drive many sectors in the modern society, such as factories, data centers, household appliances, robots, electric vehicles and aircraft, to name a few. The condition monitoring and fault detection of these machines are increasingly important to guarantee smooth operation and minimize down time, which is also made possible with the advancement of sensing technologies and the growth of internet of things. In particular for electric motors, different kinds of mechanical faults and electrical fault can happen, and eccentricity faults are among the most common, where the rotor and stator are not concentric anymore during rotation [1]. Specifically, eccentricity faults can be categorized into three types: static eccentricity, dynamic eccentricity, and mixed eccentricity. Static eccentricity occurs when the center of the rotor is deviated from the central axis of the stator bore, while the rotation center is still aligned with the center of the rotor. Dynamic eccentricity occurs when the rotation center and the stator bore central axis still align, but the rotor center is displaced. Mixed eccentricity is a combination of both static eccentricity and dynamic eccentricity [1]. There are many reasons that can cause motor eccentricity, and the air gap eccentricity can in turn damage other parts of the motor and cause breakdown of the machine if not corrected in time. During the manufacturing stage, it is not feasible to produce motors with zero air gap eccentricity. Static eccentricity may exist due to the imperfect alignment between stator core assembly and the rotation center, or the deviation of the stator core from a perfect circle. Similarly, a small dynamic eccentricity can also exist due to the imperfect alignment between center of the rotor and the rotation axis, or imperfect shape of the rotor. In most motors, while a small level of eccentricity is tolerated during manufacturing and installation stage, quality control is necessary to ensure the deviation is within a few percent. The eccentricity level can increase throughout the operating lifetime of a motor due to various reasons, such as the degradation of mechanical parts including mounting structure assembly and bearings. The air gap eccentricity induces unbalanced magnetic pull (UMP), which may cause stator winding faults and rubbing between stator and rotor with elevated eccentricity level, eventually leads to failure of the machine. It is therefore essential to inspect electric motors for eccentricity conditions for quality control in the production stage, and for safe operation and asset protection throughout the lifetime of the machines.

Electric machine fault detection has attracted significant attention in the past a couple decades, and various methods have been proposed and investigated, with sensing modalities including noise and acoustic emission [2], vibration and current [3]–[7]. Vibration analysis and motor current signature analysis (MCSA) are two major methods for eccentricity fault detection. In general, the UMP caused by eccentricity fault can cause increased vibration, which can be measured by accelerometers. Numerous signal processing techniques, and more recently machine learning and deep learning models have been developed and applied for vibration signal based electric machine fault detection and classification [8]. One problem this method faces is that many external vibration sources, such as the mechanical unbalance of the motor installation, can be mixed together in the measured vibration signal especially on the factory floor, making the identification of fault related signals more challenging. Moreover, the sensitivity of vibration

analysis also largely depends on the specific location of sensor installation. Hence it can be unreliable to identify machine faults such as eccentricity based solely on vibration signals. One consequence is that Algorithms that perform well on a particular dataset often fail to achieve similar performance on a new dataset, and therefore cannot be generally deployed [8].

Alternatively, MCSA uses stator current as its sensing modality, and has the potential to address the problems in vibration based fault detection. Since it only uses stator current signals and requires no additional sensor, MCSA is also attractive as a low-cost solution that is easy to implement. In case of eccentricity fault, the non-uniform air gap creates additional harmonics in the permeance function and air gap magnetic flux. Some of these harmonics show up in the induced voltage or back-EMF in the stator windings, and are eventually reflected in the stator current spectrum. Thorough physics-based models have been established to understand the signatures in stator current signals for each type of motor faults including eccentricity [9]–[12]. However, MCSA based eccentricity fault detection has its own challenges. While a lot of the spatial harmonics caused by eccentricity can be reflected in vibration signals, they do not show up in the time harmonics and are missing from the stator current spectrum. Moreover, the existence of certain fault signatures in stator current depends on specific motor design parameters and is not universal. For example, it has been proven that under certain stator slot and rotor bar number combinations, some signatures at slot harmonic frequencies due to static eccentricity are more difficult to detect [10], [12]. Additionally, the eccentricity fault signatures in frequency spectrum of stator current are typically a few orders smaller than the dominating fundamental component of electric supply frequency. Many machine learning models that perform well on vibration signals are not directly applicable to MCSA as they often fail to distinguish the much similar stator current signals measured at healthy and faulty conditions. Therefore, physical models based on domain knowledge typically need to be first established in order to analyze the signals and identify fault related signatures, followed by detailed spectral analysis to extract those features to be used for fault detection.

In this paper, we investigate a mathematical method, namely topological data analysis (TDA), for MCSA applications. We show that it is very effective in extracting features in stator current signals associated with eccentricity fault and distinguishing data measured at different eccentricity levels. The extracted topological features can then be used to develop data-driven models for fault detection and quantification. Compared with conventional signal processing methods, the proposed approach is model-free, and requires only a very short data sequence to effectively extract fault features and make reasonable predictions. The basic idea and procedure has been presented in our recent work [13], [14]. We have since conducted more thorough theoretical and experimental investigations to understand the capability of the method, and significant updates have been made to this extended paper.

In order to make sure the extracted topological features are indeed associated with eccentricity fault, not due to noises in the measurement, we have developed a physical model to generate simulation data under different fault conditions. We apply the same TDA procedure to the simulation data, where we are certain the only difference is from the eccentricity level, and compare the results with those obtained from the experimental data. Very similar behaviors in the obtained topological features represented by Betti sequences are obtained in the simulation case.

Previous work only studied eccentricity fault for a motor under no-load condition, while the effectiveness of the TDA based method for motors under different load conditions was not investigated. In this paper, we perform experiment and collected data for an induction motor under eccentricity faults at multiple on-load conditions. When then process the experiment data with TDA and investigate how the extracted topological features are related to different load conditions and different eccentricity levels. We also conduct various tests using machine learning models for eccentricity fault level estimation and prediction using time-domain data and TDA processed data, and show that the method is effective in extracting fault related features and enabling data-driven eccentricity fault detection for on-load conditions, including mixed load conditions. Potential applications of the method under other faulty conditions are also envisioned and discussed.

The rest of the paper is organized as follows. In Section II, we give an introduction to TDA, persistent homology, and its calculation process; in Section III we describe the experiment setup for motor stator current data acquisition under controlled eccentricity conditions; in Section IV, we apply the TDA process to the measured data from different eccentricity levels, and validate that the extracted features are indeed associated with eccentricity fault with simulation data; in Section V, we present a data-driven approach for eccentricity level prediction using the proposed TDA method and demonstrate its interpolation and extrapolation capabilities; and finally in Section VI we provide concluding remarks.

II. Topological Feature Extraction Method

In this section, we introduce the TDA method and the process of extracting topological features and generating persistence diagram and Betti sequence from a data space.

TDA offers a numerical procedure to extract shape information from a given data space, such as connected components and holes [15]. Generally, a few advantages make TDA very attractive for many challenging data analysis tasks: topological features are invariant under small and continuous deformations; they are also coordinate-free, and more robust against noises compared with other geometrical methods. In fact, in recent years, TDA is an actively pursued research area, and has been applied to a broad range of scientific problems, including image analysis [16], time-series data analysis [17], sensor networks [18], chemistry [19], material science [20], etc. These developments are largely enabled by a powerful tool named *persistent homology* [15], [21], [22].

The *homology* of a data space describes its topological features, such as connected components and holes, and *persistent homology* computes those features that persist across different scales. Rigorous mathematical formulations and detailed

descriptions can be found in multiple references [15], [21], [22]. In this paper we aim to give a brief description of the calculation procedure to obtain the *persistent homology* of a data space, which is summarized as the following four steps:

First, we represent a given data space with a *point cloud*, which is formed by a number of data points sampled from the data space. Different sampling and embedding techniques can be applied.

Second, we identify the *simplicial complex* of the point cloud, which is a collection of topological building blocks in different dimensions, or *simplices*, such as points, edges, triangles, etc. In particular, *Rips complex* is a commonly used algorithm to construct a simplicial complex, which assigns a threshold value or filtration radius r, and only includes complices with pair-wise Euclidean distance between their data points no larger than r.

Third, *homology* H_i, which counts the number of topological features, is calculated from the constructed simplicial complex, where the subscript i denotes the dimension. For instance, H_0 counts the number of connected components, and H_1 counts the number of holes.

Lastly, *persistent homology* is obtained through a filtration process of Rips complex, which computes the homology at different filtration radius r, and tracks the "birth" and "death" of each topological feature at the corresponding r. The evolution of homology across the whole range of r is recorded as persistent homology.

Multiple algorithms to perform Rips complexes filtration and persistent homology calculation have been developed, validated and implemented. In this work, we use python library *Ripser.py* for the computation of persistent homology [23]. Once calculated, persistent homology can be represented in different forms, and *persistence diagram* is a popular choice, which is composed of a set of points $(b, d)|b, d \in \mathbb{R}^2$ and $d > b$, where each point corresponds to the "birth" and "death" of one topological feature. To be more specific, each point (b, d) denoted a topological feature being "born" at radius b and "dead" at radius d.

Persistence diagram can be transformed into other representations forms, such as persistence barcode, persistence landscape, and Betti sequence. In this study, we plan to use the extracted topological features of different data for data-driven models, and it is often convenient to have them represented as vectors of the same length to serve as input data. Betti sequence, or Betti curve is a representation that effectively achieves that [24], [25]. Assume D is a persistence diagram with a finite number of off-diagonal points, with $\alpha = (b_\alpha, d_\alpha)$ a point in the diagram, and maximum filtration radius $r_{max} > 0$, let $\{r_i\}_1^M$ be equally spaced points within $[0, r_{max}]$, the Betti sequence of D is a vector of length M defined as $\vec{\beta} = (\beta_i)_1^M$, with the entries β_i count the number of points in the persistence diagram at filtration radius r_i. Define the function:

$$f_\alpha(r) = \begin{cases} 1, & b_\alpha \leq r \leq d_\alpha, \\ 0, & \text{otherwise}, \end{cases}$$

Then we can obtain the points on a Betti curve through the summation: $\beta_i = \sum_{\alpha \in D} f_\alpha(r_i)$.

While most people use TDA to reveal the major shapes in data spaces in many applications, and either ignore the smaller topological features or consider them as noises, we apply TDA in an opposite manner, by filtering out the main topology of the data space in our stator current data, and instead focusing on the smaller features. We will show that the extracted topological features are robust and quantitatively different between data obtained under different eccentricity levels. Data-driven models can then be developed for eccentricity fault prediction based on the mapping between the extracted topological features and fault severity level.

III. Experiment Setup & Data Acquisition

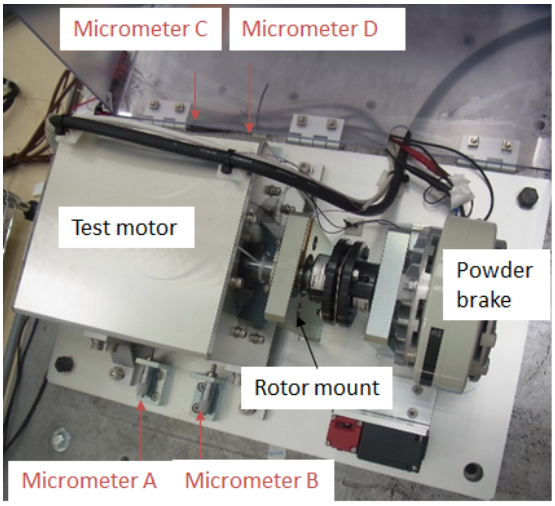

Fig. 1. The experiment setup for the study of induction motor eccentricity.

Before applying TDA, we first introduce the experiment setup and data acquisition system for obtaining stator current signals of a motor under different eccentricity conditions.

A 0.75 kW, three-phase, 2-pole-pair squirrel-cage induction motor is modified and used in our investigation, which has 36 stator slots and 28 rotor bars, and a nominal air gap size of 0.28 mm. The line-to-line voltage and frequency are 200 V and 60 Hz, respectively. As shown in Fig. 1, a few modifications are made to the motor to create different levels of static eccentricity (SE) in a controlled manner. The original bearings of the motor are removed, and the rotor is instead supported by two custom-made mounting structures (only the mounting structure on the load side is visible in the photo) through the extended rotor shaft and a pair of new bearings installed on the mounting structures. The stator assembly of the motor is mounted on a linear stage so that its position is adjustable in the horizontal direction using two pairs of micrometers. A powder brake is connected to the test motor via the shaft and serves as load. In addition, two pairs of displacement sensors have been installed on the stator facing the air gap, in order to measure the actual air gap size in both horizontal and vertical directions when the motor is running [13], [14].

With this setup, different SE levels in the horizontal direction can be created. In our experiment, a total of 6 SE levels were created when the motor is stand still: 7.1%, 16.5%,

31.1%, 42.5%, 47.5%, and 57.3% , where the percentage is defined as the ratio of the maximum air gap deviation and the nominal air gap size. For each eccentricity setting, the motor is tested under 5 different load conditions: 0 N·m, 1.3 N·m, 2.0 N·m, 2.7 N·m, 3.5 N·m. Data from three phase current sensors and four air gap sensors were recorded for each eccentricity and load setting at 10 kHz sampling frequency. From the air gap sensor readings, it was shown that the actual SE level of the air gap is very close to the original setting in each case, with variation within 3%. While dynamic eccentricity (DE) level is not adjusted in the experiment setup, we do observe a small DE of around 6% for all cases based on the air gap sensor readings. Since a small eccentricity exists even in motors considered healthy due to imperfect manufacturing and installation process [1], therefore the measured DE is reasonable. This mixed eccentricity effect creates side band signals in the stator current spectrum at

$$f_c = f_s \pm f_r = \left(1 \pm \frac{1-s}{p}\right) f_s \tag{1}$$

and the higher harmonics. The amplitude of side band signals increases with increasing eccentricity level (see, for example Ref. [3]). Here $f_s = 60$ Hz is the supply frequency, f_r is the rotation frequency, and $p = 2$ is the pole pair number of the induction motor. Slip s depends on the load condition, and increases with higher load.

With 6 different SE conditions, and 5 different load conditions, data are recorded for a total of 30 test conditions. Due to this large number of test conditions, in the subsequent analysis, we will only show data from the most representative cases.

For a comparison of the obtained stator current signals under different test conditions, the time-domain and frequency-domain phase A current signals at the smallest (7.1%) and largest (57.3%) SE level, under smallest (0 N·m) and largest (3.5 N·m) load conditions respectively are plotted in Fig. 2. As shown in Fig. 2(a), current amplitude increases at on-load compared with no-load condition; however, the time-domain waveform is dominated by the fundamental component and it is hard to distinguish the different eccentricity cases under the same load condition. Detailed spectral analysis is needed to identify the components related to eccentricity faults. Fig. 2(b) shows the frequency spectrum obtained from 60s-long time-domain signal for each case in order to resolve the fault signals and their harmonics. Zooming in to the lower side band corresponding to (1), we can observe from Fig. 2(c) two things: one, the peak value of the component at higher SE level is higher; two, the frequency increases from close to 30 Hz to around 30.8 Hz when the load condition changes from 0 to 3.5 N·m as the slip s increases.

IV. TDA on Eccentricity Data

In this section, we perform TDA on the experiment data under eccentricity, show that eccentricity related features can be obtained with the process. We further present a simulation model of motor under eccentricity fault built on modified winding function method, and validate our findings with TDA using simulation data.

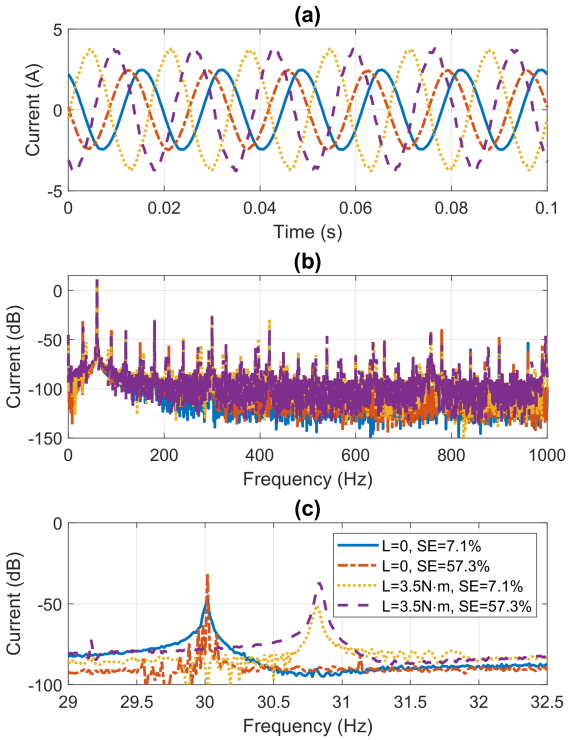

Fig. 2. Phase A current signals measured under 4 different test conditions listed in subfigure (c). (a) a segment of time-domain signals, (b) frequency spectra obtained from Fourier transform using 60 s of time-domain data, and (c) zoom-in around lower side-band $f_s - f_r$.

A. Experiment Data Analysis

We apply the TDA process described in Section II to the measured stator current signals.

A point cloud is naturally formed by sampling the recorded three-phase current data segment and placing them in 3D Euclidean space. For each case, we take a segment of 1024 consecutive data points from the stator current data. Since the data is measured at 10 kHz sampling frequency, the segment of 1024 points corresponds to about 0.1 s measurement in time domain. One data segment is also called one sample in the subsequent analysis. The point clouds of the data segment from the four test conditions corresponding to Fig. 2 are shown in Fig. 3. Since the dominating component of the signals is a periodic wave of fundamental frequency, the most significant shape is a large circle in 3D space. For an ideal sinusoidal signals, the point cloud forms a perfect circle; when other frequency components exist, the points would deviate from the perfect circle. Since the fault components are much smaller in amplitude, it is difficult to tell the different eccentricity levels from the point cloud shapes alone. For on-load conditions, the radius of the circle increases, as shown in Fig. 3(c) and (d). For subsequent TDA process, we normalize each data segment to its maximum value to account for the change in current amplitude at different load conditions.

With the point clouds, we can proceed with the homology computation and obtain persistence diagrams. Fig. 4 shows

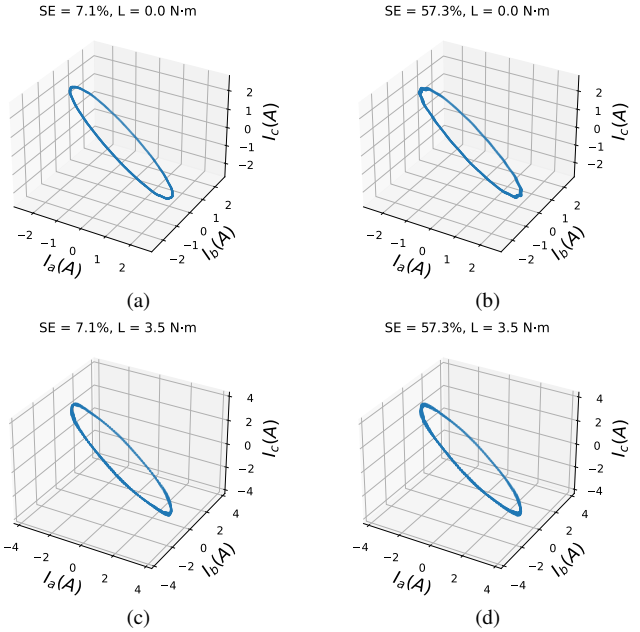

Fig. 3. Point clouds of three-phase stator current data segments corresponding to the four test conditions: (a) SE 7.1%, no load, (b) SE 57.3%, no load, (c) SE 7.1%, load 3.5 N·m, and (d) SE 57.3%, load 3.5 N·m.

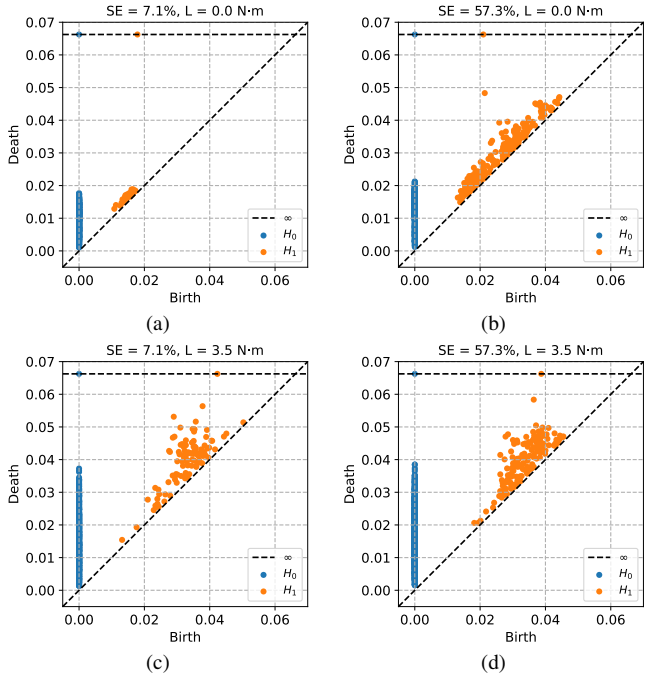

Fig. 4. Computed persistence diagrams for both H_0 and H_1 features from phase current data segments corresponding to the four test conditions shown in Fig. 2.

the computed H_0 and H_1 persistence diagrams corresponding to the aforementioned four conditions. The most noticeable differences lie in the H_1 features, which correspond to the small holes formed by neighboring points in the point clouds during the filtration process. For an ideal sinusoidal wave, only one large hole is formed by its point cloud. With phase current data under eccentricity fault, the point cloud deviates from the ideal circle due to the many frequency components that exist in the data. When the eccentricity level is small, the deviation is also small, and only a few features are formed in the H_1 diagram; when the eccentricity level increases, the deviation of the points from the ideal circle is larger, and these points are more likely to form small circles during the filtration process. Therefore more and more features show up in the H_1 diagrams with increasing eccentricity level. In addition, more features show up at on-load conditions, as shown in Fig. 4(c) and (d). Many features also tend to be further away from the diagonal line compared with the no-load cases, meaning their lifespan is longer. This is due to the fact that many harmonic components in the current increases under high load, creating additional topological features in the data space. For H_0 features, which are the connected components or clusters in a point cloud, the difference is not as visible as the H_1 diagram, since they all fall on one single line. The difference in H_0 will be more straightforward when represented in Betti sequences, which will be presented in the following paragraph.

Persistence diagram is an important visualization tool for homology, but not quite convenient as input of machine learning models. Next we convert the diagrams into Betti sequences of the same lengths: for both H_0 and H_1 sequences, the length is fixed at 1024 whereas the filtration ranges are of [0, 0.045] and [0, 0.07] respectively. Fig. 5 show the computed Betti sequences from the corresponding persistence diagrams

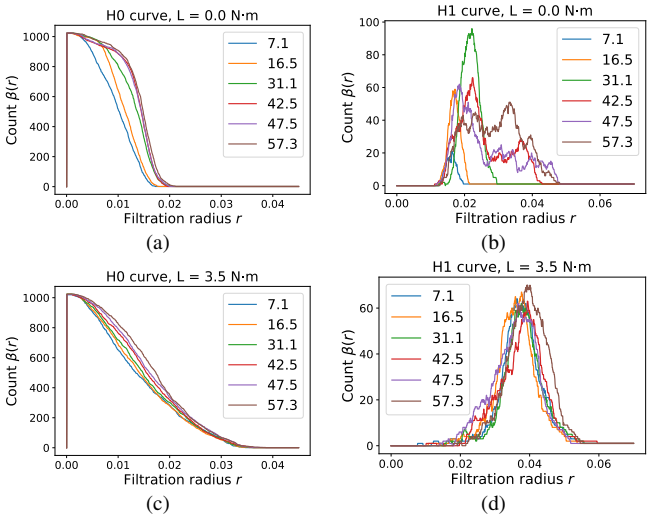

Fig. 5. (a) H_0 and (b) H_1 Betti curves calculated from measured stator current data at different SE levels under no-load condition; (c) and (d) are H_0 and H_1 Betti curves for data at different SE levels measured at 3.5 N·m load respectively. Legend of each figure indicates corresponding SE level in percentage.

for data at different SE levels at both no-load and on-load conditions. While we cannot easily tell the differences of H_0 features from the persistence diagrams, we can observe the trend in the H_0 Betti curves. When the filtration radius is 0, all 1024 data points are separate, therefore all the Betti curves start at 1024. Upon increasing filtration radius, more and more neighboring points are connected; therefore the number of H_0 features starts to decrease, eventually all points are connected and there is only one feature left. With higher eccentricity level, the amplitude of fault components increases, and the

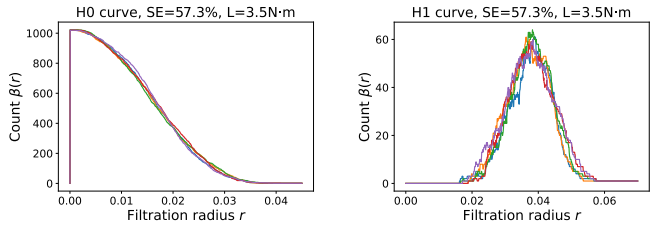

(a) (b)

Fig. 6. (a) H_0 (a) and (b) H_1 Betti curves corresponding to five different data segments from the same test condition with SE level 57.3% and load 3.5 N·m.

data points are further apart from one another due to their deviation from the large circle (see Fig. 3); therefore the points are connected at a later stage and these H_0 features survive longer, and the area under H_0 Betti curve is monotonically increasing with eccentricity level.

From the H_1 Betti curves, we can see that the number of features as a function of filtration radius changes with eccentricity levels, and the peak position of the curves seems to correlate with the SE level: peak shifts to higher filtration radius r at higher SE level. These observations are more visible at no-load condition as shown in Fig. 5 (a) and (b). At on-load condition, the change in topological features embedded in the measured signal is significant compared with the data from no-load case under the same SE fault, which is reflected in the line shape of the Betti curves shown in Fig. 5 (c) and (d). Consequently, the difference between data from different SE levels is not as distinct as the no-load cases. However, the same trends are still visible for both H_0 and H_1 curves.

Another important merit of persistent homology is its robustness to noises: similar data structures yield similar persistent homology. To verify, we compare the Betti curves obtained from multiple data segments measured at the same test condition. Fig. 6 show the Betti curves of five different data segments at SE level 57.3% and load 3.5 N·m, and they are quite consistent. The similarity of these Betti curves implies that the temporal fluctuations between different samples of time-domain data are filtered out by the proposed calculation procedure, and one could stably extract the fault signature with a relatively short segment of data of around 0.1 s.

Based on the above analysis, we conclude that the persistent homology and Betti curves can effectively differentiate data from different test conditions, while reliably providing similar output for data from the same test condition.

B. Verification with Simulation Data

In order to verify that the differences observed in the Betti curves are indeed due to the difference in eccentricity, we have developed a numerical model and generated simulation data under different eccentricity conditions corresponding to experiment settings, and implemented the same TDA process to compare with experiment results.

The numerical model takes in parameters including motor design parameters, supply voltage, load condition and fault condition, calculates the inductance terms between rotor and stator windings of the motor for each rotor position, and updates the dynamic signals during the operation of the motor including stator current, speed, and torque. Signal processing techniques such as FFT can then be applied to the simulated stator current signal in order to obtain the frequency spectrum. All signal components related to eccentricity faults can then be identified.

The motor dynamics are described by coupled circuit equations. The inductance terms and their derivatives, which are critical in determining the motor current and torque, are calculated using modified winding function method (MWFM) and updated at each rotor position [10], [12], [26]. For winding i and winding j, the inductance is evaluated as

$$L_{ij}(t) = \mu_0 lr \int_0^{2\pi} n_i(\phi,t) M_j(\phi,t) g^{-1}(\phi,t) \mathrm{d}\phi, \quad (2)$$

where μ_0 is the free-space permeability, r is motor radius at the air gap, l is the stack length, $n_i(\phi,t)$ is the winding turns function for winding i, and $M_j(\phi,t)$ is the modified winding function for winding j. From the equation, we can see that the air gap function $g(\phi,t)$, which describes the spatial and temporal air gap profile, is especially important in calculating the motor performance under eccentricity conditions. Under SE and DE conditions, the air gap function can be written as:

$$g(\phi,t) = g_0 K_c - \delta_{SE} g_0 \cos(\phi) - \delta_{DE} g_0 \cos(\phi - \omega_r t). \quad (3)$$

where g_0 is nominal air gap length, K_c is Carter's coefficient to quantify the slotting effect, δ_{SE} and δ_{DE} are the SE and DE amplitude respectively. Detailed modeling process is described in Ref. [27].

Dynamic simulations can then be conducted to obtain the motor current signals at each condition. Fig. 7 shows the simulated time-domain signal and the frequency spectrum of stator current with SE level of 42.5% and DE level of 6% under no-load condition, together with the corresponding experiment data. While the simulation does not match exactly with experiment, due to unavoidable simplifications in the model, key features of the signal due to eccentricity can be identified with good accuracy: the time-domain waveform and amplitude match well with experiment, the low frequency sideband signals corresponding to (1) show up in the simulated spectrum with good agreement with experiment. Therefore the simulation model is sufficient for investigating motor under different fault conditions that can be difficult to create experimentally and subject to uncertainties in the measurements.

By changing the air gap profile in (3) while keeping all other settings the same, we can simulate current signals at different eccentricity levels. With the simulated data, we know for sure that any difference in data obtained under different settings is due to eccentricity only.

We run simulations at eccentricity conditions corresponding to the experimentally measured values, obtain the stator current data with the same sampling rate of 10 kHz for each case, and process the simulated data with the same TDA procedure as the experiment data , in order to validate our observations from TDA with experiment data.

Fig. 8 shows the converted Betti curves for simulation data obtained at all SE levels for both no-load and on-load conditions. Comparing Fig. 8 with Fig. 5, we can see that,

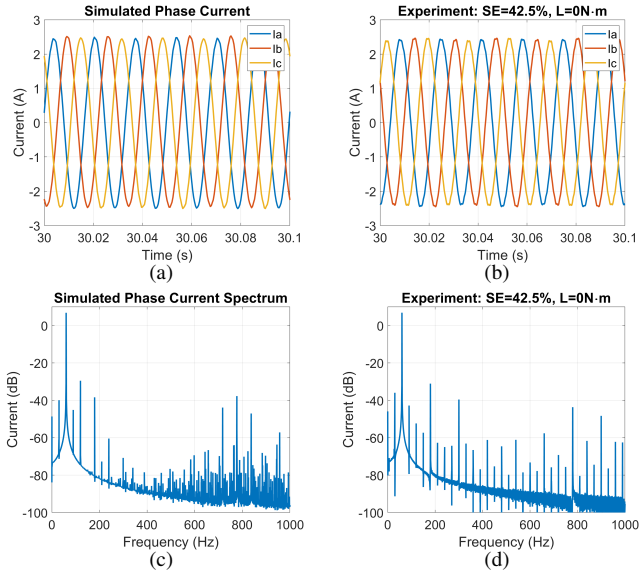

Fig. 7. The simulated ((a), (c)) and corresponding experiment measurement ((b), (d)) of phase current signal in time-domain and frequency-domain with SE level of 42.5% under no-load condition.

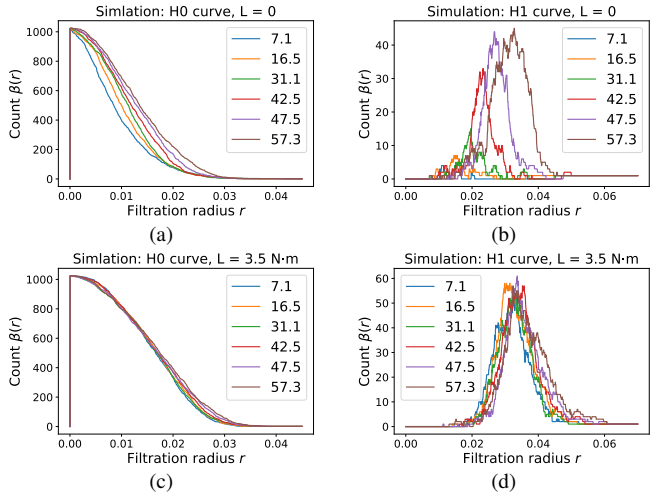

Fig. 8. (a) H_0 and (b) H_1 Betti curves calculated from simulated stator current data at different SE levels under no-load condition; (c) and (d) are H_0 and H_1 Betti curves for data at different SE levels measured at 3.5 N·m load respectively. Legend of each figure indicates corresponding SE level in percentage.

while the line shapes do not match exactly between simulation and experiment data, the changes in the curves with increasing eccentricity level have the same trend. For H_0 curves, the data points are generally further apart in the point cloud at higher fault level, causing the features to disappear at a larger filtration radius, therefore the area under H_0 curve monotonically increases with increasing eccentricity level. Similarly for H_1 curves, very few features exist at small fault levels throughout the filtration process, while more features appear due to the increased fault level. The peak position of H_1 curve appears at larger filtration radius for larger SE level. For on-load conditions, as shown in (c) and (d) of Fig. 8 and Fig. 5, the topological features are largely dominated by the load, and the variations due to different SE fault is not as obvious as no-load conditions. However the trend for both H_0 and H_1 curves is still visible.

With the comparison between simulation and experiment, we can conclude that the extracted features through the TDA process can be a good indication of eccentricity fault. While noises exist in the experimentally measured data, they do not hinder the effective extraction of topological features relevant to the eccentricity fault, as verified by both the robustness of the experiment data as shown in Fig. 6, and the comparison with simulation data as shown in Fig. 8.

V. TDA for Eccentricity Level Prediction

From above analysis, we can see that TDA is effective in revealing small fault signatures embedded in a large background signal, and separating signals from different fault levels. In this section, we present a data-driven approach of eccentricity fault detection, quantification, and prediction based on TDA.

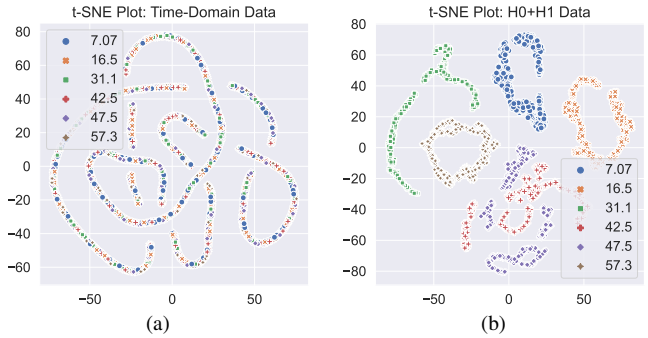

Fig. 9. t-SNE plot in 2d for (a) time-domain phase current data, and (b) H_0 and H_1 sequences combined for different SE levels under no-load condition.

First we process and analyze the data. The experiment data measured at each SE level and each load condition is segmented into a total of 1170 samples, each of length 1024. Same data segmentation is done for all 30 test conditions, making the total number of data segments 35100. As discussed in earlier sections, the time-domain data are dominated by the fundamental component at supply frequency, and in sinusoidal waveform for all test cases. There is no noticeable difference between data from different SE levels under the same load condition. For data from different load conditions, the current amplitude will be different. A few exemplar data segments for phase A current have been shown in Fig. 2(a). Another example data segment for three-phase current has been shown in Fig. 7(b). We will refer the segmented time-domain data as TD dataset.

After data segmentation, we then apply the established TDA procedure to obtain Betti sequences for all these data samples, as detailed in Section IV-A. For each time-domain data segment, we calculate its H_0 and H_1 sequences. For convenience, we make the length of each H_0 and H_1 sequence to be 1024. Corresponding to TD dataset, we refer the compiled Betti sequences as H_0 and H_1 dataset.

To visualize the differences of data at different eccentricity levels, in Fig. 9 we show the t-distributed stochastic neighbor embedding (t-SNE) plot [28], which is a commonly used

tool to represent similarities of high-dimensional data in low dimension, of both time-domain phase current data and their corresponding Betti sequences under no-load condition. With time-domain data, samples from all eccentricity levels are mixed together with no clear clustering, indicating these data segments are highly similar. The reason is that they are dominated by the large 60 Hz signal, as shown in Fig. 2. For Betti sequences, however, the data samples do cluster according to their respective eccentricity level. We point out that the dominant 60 Hz signal only corresponds to the feature value at very large filtration distance in H_1 Betti sequences, due to the large hole in the point clouds shown in Fig. 3, and has little impact on the profile of the Betti curve. In this sense, the thresholded Betti curve serves as a "nudge filter" that effectively removes the dominant time-domain signal, and magnifies the behavior of small signals where the fault signatures reside.

In this work, we demonstrate that with an effective feature extraction method, complicated machine learning models and deep learning models are not needed for data-driven fault detection and quantification. Only simply regression models will be used in the following tests.

For practical motor eccentricity fault detection applications, we can envision two different scenarios, one in the manufacturing and assembling stage, the other throughout the operation lifetime of the motor.

A. Scenario I: SE Level Estimation

In the manufacturing stage, the main goal is to inspect the manufactured and assembled motors for quality control, to ensure the eccentricity level is below a threshold value. Since a large number of motors of the same model will be mass produced in the factory, it makes sense to collect data covering a wide range of eccentricity conditions with a test motor, and develop a data-driven model to make predictions on the eccentricity level using new data measured on other motors of the same type.

To mimic this scenario, we shuffle the data from all eccentricity levels and split them into training and test sets, with a split ratio of 80:20. The same shuffling and splitting process is applied to TD, H_0, and H_1 datasets. Models will be trained and tested on each type of data separately, as well as combined H_0 and H_1 (referred to as $H_0 + H_1$) for comparison. In addition, we train and test models with data for each separate load condition, as well as for all load conditions to evaluate the impact of load to the prediction performance.

While many different models can be developed, we show the results from simple k-nearest neighbor (k-NN) regression models [29] to demonstrate the capability of TDA. For a given new data sample, the k-NN algorithm simply search for its nearest neighbors from the training data, and predict the eccentricity level using the average level of these neighbors. We implemented the algorithm using *scikit-learn* [30] library in Python. Standard Euclidean distance is used in searching for nearest neighbors. All points in each neighborhood are weighted equally for prediction. During training, we compare the prediction of SE level from the model and ground truth, and find the optimal number of nearest neighbors to minimize the root-mean-squared-error (RMSE). During testing, we evaluate each model performance by calculating the root-mean-squared-error (RMSE) and mean-absolute-error (MAE) on test data.

The results of calculated MAE for trained models are summarized in Table I. For each load condition, as marked in bold font, the best model performance on estimating the SE level of test data is from model trained with H_0 and H_1 Betti sequences combined. In particular, at no-load condition, the trained model can make perfect prediction with 0 error. The MAE error increases slightly at higher load conditions, which is still well below 3%. When all five load conditions are considered together, the test MAE error is only slightly above 1%. On the other hand, the models trained with raw TD data always perform worst.

TABLE I
MEAN ABSOLUTE ERROR (MAE) OF SE LEVEL ESTIMATION WITH K-NN MODELS TRAINED ON TIME-DOMAIN (TD) CURRENT DATA AND BETTI SEQUENCE DATA RESPECTIVELY, UNDER DIFFERENT LOAD CONDITIONS.

Load (N·m)	TD	H_0	H_1	H_0 + H_1
0	6.89	0.38	0.01	**0.00**
1.3	6.58	0.58	2.93	**0.31**
2.0	10.45	1.40	1.31	**0.53**
2.7	12.99	2.33	5.79	**2.06**
3.5	13.89	2.78	6.13	**2.35**
All	10.82	2.3	4.6	**1.12**

We can further visualize the model performance with violin plot, which shows the distribution of predicted SE values for data from each SE level. The results for models with data from all load conditions, which correspond to the last row in Table I, are plotted in Fig. 10. For each SE level, the horizontal marker shows the mean of predicted SE value over all test data samples, and the probability density is added in shaded blue to show how the prediction values are distributed. As we can see, the model performs poorly with TD data, and the mean for each SE level is far from the true value. With H_0 and H_1 data alone, the model performance is already much improved. While the mean is very close to the true value, there are some outliers as shown in the probability density. When both H_0 and H_1 data are used, best performance is reached with minimal error.

B. Scenario II: SE Level Prediction

On the other hand, during the service of a motor, it is not possible have measurement data for all possible eccentricity levels. Instead, we expect to have measurement data collected during inspections, when eccentricity level is still low. A data-driven model can be built based on these earlier measurements, and used to predict the eccentricity level during subsequent measurements where the fault is expected to become more severe over time.

Such extrapolation task to unseen data is challenging for all machine learning and deep learning models. For this task, we assign the experiment data from the four smaller SE levels with nominal SE levels 7.1%, 16.5%, 31.1%, 42.5% as

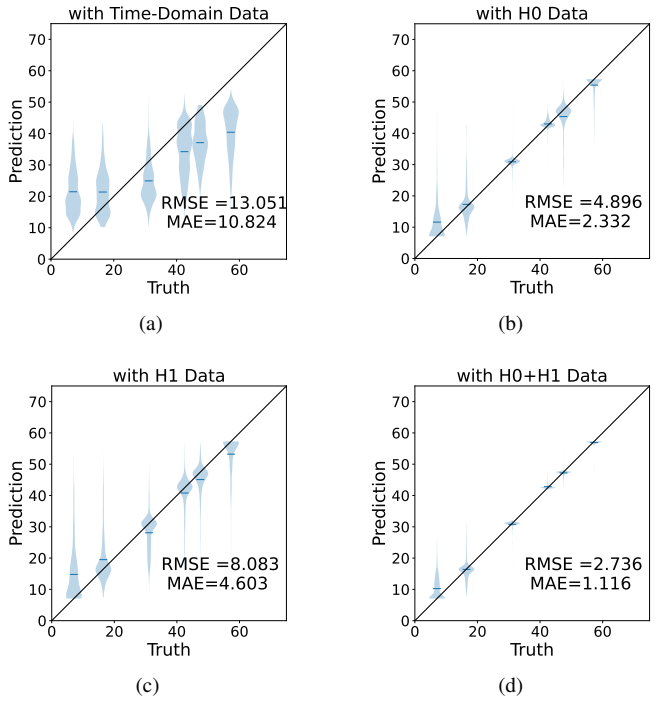

Fig. 10. Violin plot for SE level estimation using k-NN model trained with data from all SE and load conditions using (a) phase current data, (b) H_0 Betti sequences, (c) H_1 Betti sequences, and (d) both H_0 and H_1 Betti sequences.

training dataset. Data from the two higher SE levels, namely 47.5%, and 57.3% are not used in the training, and are reserved as test dataset, to check the prediction capability of the trained models. Again, data from each test condition have been segmented into 1170 samples of length 1024. Similar to the previous task, we train models using data under each load condition, as well as data from all load conditions, in order to understand the capability of TDA. Again, four types of data, namely raw TD data, H_0 Betti sequence, H_1 Betti sequence, and combined $H_0 + H_1$ sequences, are used to train models separately and their performances are compared.

To develop an effective regression model, we extract the features associated with SE fault in the Betti curves identified in Section IV: for H_0 curve, we use the total area under the curve; for H_1 curve, we use the peak position of the curve. For time-domain data, we extract the RMS value of the phase current. Quadratic regression models are trained respectively using these features. During training, we find the coefficients of the quadratic function that best fits the training dataset. The trained regression models are then tested on the corresponding test dataset. The MAE for SE level prediction of each trained model on test data is summarized in Table II. For each load condition, models trained with TD data perform poorly, with MAE over 27% for all cases. With H_0 Betti squence data the model peroformance is much improved for all the load conditions. While H_1 feature is not as effective for the prediction task on new data, it is still better than using raw TD data; and combining H_1 with H_0 data can achieve similar result or further improve the result.

Depending on the application, a motor can operates at constant load conditions, or with mixed load conditions during the life time. As shown in Table II, for constant load conditions, the proposed method generally works better for eccentricity level prediction. Fig. 11 shows the performance of regression models trained on data collected at the same load condition of 2.0 N·m with different input data type. With TD data, the model essentially cannot distinguish data from different SE levels. With converted Betti sequence data, the prediction accuracy is much improved. With combined H_0 and H_1 Betti curve data, the prediction RMSE is reduced to about 4% and the MAE is even lower.

TABLE II
MEAN ABSOLUTE ERROR (MAE) OF SE LEVEL PREDICTION ON UNSEEN DATA FROM NEW SE CONDITIONS WITH REGRESSION MODELS TRAINED ON TIME-DOMAIN (TD) CURRENT DATA AND BETTI SEQUENCE DATA RESPECTIVELY, UNDER DIFFERENT LOAD CONDITIONS.

Load (N·m)	TD	H_0	H_1	H_0 + H_1
0	28.22	10.22	12.48	**10.10**
1.3	27.56	**3.91**	10.77	3.93
2.0	27.3	3.81	8.5	**3.29**
2.7	28.05	**2.87**	20.94	3.14
3.5	27.36	**3.40**	21.76	3.43
All	27.92	16.74	21.32	**13.6**

Among these tests, the mixed load condition, which corresponds to the last row in Table II, is considered to be most challenging, as the small differences in SE level is largely masked by the varying load condition. The performance of the trained models are plotted in Fig. 12. With TD data, the model cannot distinguish data from different SE levels, and the mean prediction value is far from the truth. With Betti sequence data, especially H_0 and combined H_0 and H_1 the prediction is much closer to the true value.

C. Discussions

Compared with MCSA, which requires involved domain knowledge and physical model to identify fault signatures, no physical model for the fault is required in the proposed method. In addition, the good prediction results can be achieved with only a short segment of time-domain data. In all the tests, the length of time-domain data is 1024 points, or about 0.1s. In comparison, traditional spectral analysis methods with MCSA often require tens of seconds or longer data in order to accurately identify the fault components, on top of the domain knowledge required to identify these fault signatures. Although the paper focused on induction motor eccentricity fault level prediction, these advantages of TDA make it promising to be applied to a broad range of fault detection tasks. A few applications and future research directions can be envisioned and are briefly discussed below.

In practice, a number of faults can occur in induction motors, such as bearing fault, inter-turn short circuit in stator windings, broken bar, etc. When multiple faults exist in a motor, fault classification is a desirable fault detection solution especially for data-driven approaches. This task has a lot of similarities to scenario I discussed in Section V-A. With TDA-processed inputs, data cluster properly according to the fault

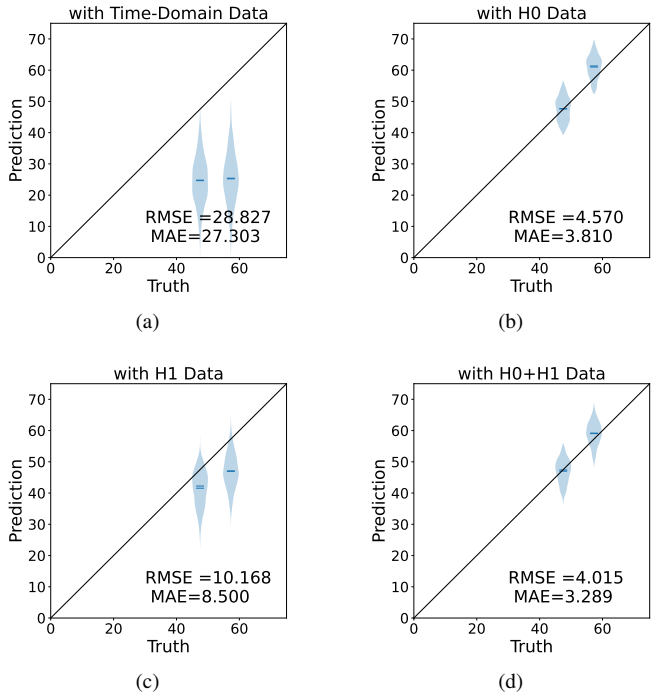

Fig. 11. Violin plot of the prediction of SE level on unseen data from new SE conditions for regression models trained on data from first four SE levels at the same load condition of 2.0 N·m using (a) phase current data, (b) H_0 Betti sequences, (c) H_1 Betti sequences, and (d) both H_0 and H_1 Betti sequences.

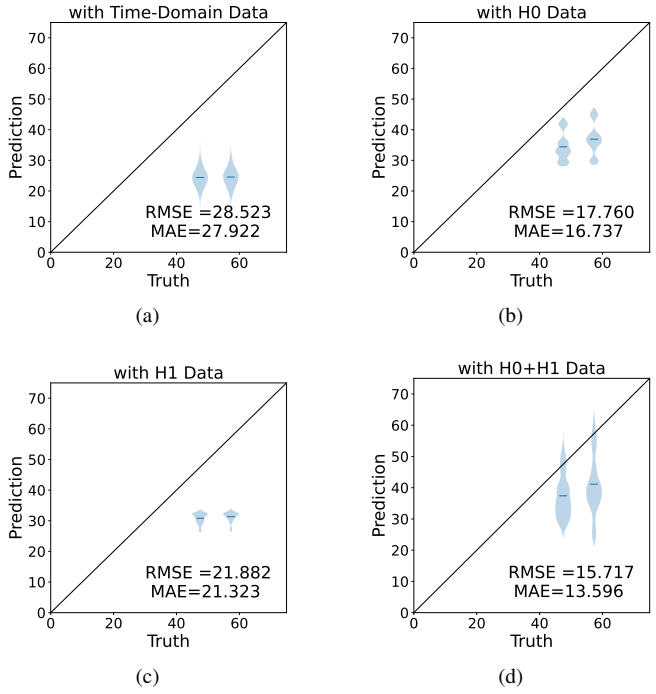

Fig. 12. Violin plot of the prediction of SE level on unseen data from new SE conditions for regression models trained on data from first four SE levels at different load conditions using (a) phase current data, (b) H_0 Betti sequences, (c) H_1 Betti sequences, and (d) both H_0 and H_1 Betti sequences.

level, even the differences are subtle, as indicated in Fig. 9, suggesting the feasibility of effective unsupervised learning with TDA processed data for fault classification. Even under various load conditions, where the topological features in the measurement data are largely modified, such clustering effect is still effective, as shown in subsequent tests shown in Table I. In addition, each type of motor fault presents its own characteristics in stator current signals (see [3], [4] for detailed analysis), and the differences between different types of faults are generally more significant than the difference between data from different severity levels of the same fault condition. We therefore expect that the TDA process can greatly facilitate the distinction of data from different fault conditions and hence fault classification tasks.

Another application is fault quantification when another fault exists at the same time. For scenario I discussed in Section V-A, where all conditions can be measured and used to train a machine learning model, we expect good results using TDA processed data. We have already added another variable in load condition as shown in Table I, and the fault level estimation remains excellent under various load conditions. Such strong clustering capability of TDA processed data remains even when another fault exists. For scenario II discussed in Section V-B, which predicts fault level for unseen data, things are more complicated. As can be seen in Table II, while the results are excellent for fixed load conditions with models trained with Betti sequence, the result of the mixed load condition is much worse. This is because the effective extrapolation of the regression model relies on the monotonically increasing features revealed in the Betti curves, and the varying load condition greatly modifies the features associated with the curves. The existence of another fault adds an additional variable, and can reduce the prediction accuracy. How large the impact of the additional fault is to the prediction accuracy depends on the fault type and severity.

As a future research direction, further theoretical and experimental investigations are desired to validate the effectiveness of TDA under these conditions. In addition, features extracted with TDA can be used in conjunction with those extracted by other methods to further improve the prediction accuracy of fault detection tasks.

VI. Conclusions

In this paper, we investigated the method of using topological data analysis for induction motor eccentricity fault level prediction under various load conditions. The procedure of extracting topological features of time-domain phase current data and converting them into vectorized Betti sequence was presented and applied to the analysis of measurement data from different fault levels. We showed that this model-free method is effective in extracting small topological features in a data space and distinguishing data from different eccentricity conditions that look very similar in the time-domain. We applied a winding function based model to generate simulation data at different eccentricity levels to exclude the impact of potential noises in the experiment setup, and verified that the extracted topological features are indeed associated with the eccentricity fault. Experiment data of different eccentricity levels from various load conditions were analyzed with the TDA method and applied for data-driven motor fault detection

and quantification tasks. We showed that the TDA processed data can greatly improve the accuracy of machine learning models for eccentricity level prediction with both interpolation and extrapolation tasks under various load conditions. The proposed method can be potentially applied to other data-driven fault detection and classification problems.

VII. Acknoledgement

The authors thank Lei Zhou, Mesaad W. Albader, and AKM Khaled Ahsan Talukder for helpful discussions.

References

[1] W. T. Thomson and I. Culbert, *Current signature analysis for condition monitoring of cage induction motors: Industrial application and case histories*. John Wiley & Sons, 2017.

[2] O. AlShorman, F. Alkahatni, M. Masadeh, M. Irfan, A. Glowacz, F. Althobiani, J. Kozik, and W. Glowacz, "Sounds and acoustic emission-based early fault diagnosis of induction motor: A review study," *Advances in Mechanical Engineering*, vol. 13, no. 2, p. 1687814021996915, 2021. [Online]. Available: https://doi.org/10.1177/1687814021996915

[3] M. E. H. Benbouzid, "A review of induction motors signature analysis as a medium for faults detection," *IEEE transactions on industrial electronics*, vol. 47, no. 5, pp. 984–993, 2000.

[4] S. Nandi, H. A. Toliyat, and X. Li, "Condition monitoring and fault diagnosis of electrical motors – a review," *IEEE transactions on energy conversion*, vol. 20, no. 4, pp. 719–729, 2005.

[5] X. Li, Q. Wu, and S. Nandi, "Performance analysis of a three-phase induction machine with inclined static eccentricity," *IEEE Transactions on Industry Applications*, vol. 43, no. 2, pp. 531–541, 2007.

[6] J. Faiz and B. M. Ebrahimi, "Static eccentricity fault diagnosis in an accelerating no-load three-phase saturated squirrel-cage induction motor," *Progress in electromagnetics research*, vol. 10, pp. 35–54, 2008.

[7] M. Akar, "Detection of a static eccentricity fault in a closed loop driven induction motor by using the angular domain order tracking analysis method," *Mechanical Systems and Signal Processing*, vol. 34, no. 1-2, pp. 173–182, 2013.

[8] S. Zhang, S. Zhang, B. Wang, and T. G. Habetler, "Deep learning algorithms for bearing fault diagnostics – a comprehensive review," *IEEE Access*, vol. 8, pp. 29 857–29 881, 2020.

[9] H. A. Toliyat, M. S. Arefeen, and A. G. Parlos, "A method for dynamic simulation of air-gap eccentricity in induction machines," *IEEE transactions on industry applications*, vol. 32, no. 4, pp. 910–918, 1996.

[10] S. Nandi, S. Ahmed, and H. A. Toliyat, "Detection of rotor slot and other eccentricity related harmonics in a three phase induction motor with different rotor cages," *IEEE Transactions on Energy Conversion*, vol. 16, no. 3, pp. 253–260, 2001.

[11] J. Faiz, B. M. Ebrahimi, B. Akin, and H. A. Toliyat, "Comprehensive eccentricity fault diagnosis in induction motors using finite element method," *IEEE Transactions on Magnetics*, vol. 45, no. 3, pp. 1764–1767, 2009.

[12] L. Zhou, B. Wang, C. Lin, H. Inoue, and M. Miyoshi, "Static eccentricity fault detection for psh-type induction motors considering high-order air gap permeance harmonics," in *2021 IEEE International Electric Machines & Drives Conference (IEMDC)*. IEEE, 2021, pp. 1–7.

[13] B. Wang, C. Lin, H. Inoue, and M. Kanemaru, "Topological data analysis for electric motor eccentricity fault detection," in *IECON 2022 â 48th Annual Conference of the IEEE Industrial Electronics Society*, 2022, pp. 1–6.

[14] B. Wang, H. Inoue, and M. Kanemaru, "Motor eccentricity fault detection: Physics-based and data-driven approaches," in *2023 IEEE 14th International Symposium on Diagnostics for Electrical Machines, Power Electronics and Drives (SDEMPED)*, 2023, pp. 42–48.

[15] C. Gunnar, "Topology and data," *Bulletin of the American Mathematical Society*, vol. 46, no. 2, pp. 255–308, 2009.

[16] T. Qaiser, Y.-W. Tsang, D. Taniyama, N. Sakamoto, K. Nakane, D. Epstein, and N. Rajpoot, "Fast and accurate tumor segmentation of histology images using persistent homology and deep convolutional features," *Medical image analysis*, vol. 55, pp. 1–14, 2019.

[17] F. A. Khasawneh and E. Munch, "Chatter detection in turning using persistent homology," *Mechanical Systems and Signal Processing*, vol. 70, pp. 527–541, 2016.

[18] V. De Silva and R. Ghrist, "Coverage in sensor networks via persistent homology," *Algebraic & Geometric Topology*, vol. 7, no. 1, pp. 339–358, 2007.

[19] Y. Lee, S. D. Barthel, P. Dłotko, S. M. Moosavi, K. Hess, and B. Smit, "Quantifying similarity of pore-geometry in nanoporous materials," *Nature communications*, vol. 8, no. 1, pp. 1–8, 2017.

[20] Y. Hiraoka, T. Nakamura, A. Hirata, E. G. Escolar, K. Matsue, and Y. Nishiura, "Hierarchical structures of amorphous solids characterized by persistent homology," *Proceedings of the National Academy of Sciences*, vol. 113, no. 26, pp. 7035–7040, 2016. [Online]. Available: https://www.pnas.org/content/113/26/7035

[21] H. Edelsbrunner, D. Letscher, and A. Zomorodian, "Topological persistence and simplification," in *Proceedings 41st annual symposium on foundations of computer science*. IEEE, 2000, pp. 454–463.

[22] A. Zomorodian and G. Carlsson, "Computing persistent homology," *Discrete & Computational Geometry*, vol. 33, no. 2, pp. 249–274, 2005.

[23] C. Tralie, N. Saul, and R. Bar-On, "Ripser.py: A lean persistent homology library for python," *The Journal of Open Source Software*, vol. 3, no. 29, p. 925, Sep 2018. [Online]. Available: https://doi.org/10.21105/joss.00925

[24] F. Chazal and B. Michel, "An introduction to topological data analysis: fundamental and practical aspects for data scientists," *arXiv preprint arXiv:1710.04019*, 2017.

[25] Y. Umeda, J. Kaneko, and H. Kikuchi, "Topological data analysis and its application to time-series data analysis," *Fujitsu Scientific & Technical Journal*, vol. 55, no. 2, pp. 65–71, 2019.

[26] N. A. Al-Nuaim and H. Toliyat, "A novel method for modeling dynamic air-gap eccentricity in synchronous machines based on modified winding function theory," *IEEE Transactions on energy conversion*, vol. 13, no. 2, pp. 156–162, 1998.

[27] B. Wang, M. W. Albader, H. Inoue, and M. Kanemaru, "Induction motor eccentricity fault analysis and quantification with modified winding function based model," in *2022 25th International Conference on Electrical Machines and Systems (ICEMS)*, 2022, pp. 1–6.

[28] L. Van der Maaten and G. Hinton, "Visualizing data using t-sne." *Journal of machine learning research*, vol. 9, no. 11, 2008.

[29] C. M. Bishop, *Pattern Recognition and Machine Learning (Information Science and Statistics)*. Berlin, Heidelberg: Springer-Verlag, 2006.

[30] F. Pedregosa, G. Varoquaux, A. Gramfort, V. Michel, B. Thirion, O. Grisel, M. Blondel, P. Prettenhofer, R. Weiss, V. Dubourg, J. Vanderplas, A. Passos, D. Cournapeau, M. Brucher, M. Perrot, and E. Duchesnay, "Scikit-learn: Machine Learning in Python," *Journal of Machine Learning Research*, vol. 12, pp. 2825–2830, 2011. [Online]. Available: http://jmlr.org/papers/volume12/pedregosa11a/pedregosa11a.pdf

Bingnan Wang received his B.S. degree from Fudan University, Shanghai, China, in 2003, and Ph.D. degree from Iowa State University, Ames, IA, USA, in 2009, both in Physics. He has been with Mitsubishi Electric Research Laboratories (MERL), located in Cambridge, Massachusetts since then, and is now a Senior Principal Research Scientist. His research expertise includes electromagnetics and photonics, and has worked on projects from wireless power transfer, sensing, to electric machines and energy systems. His current research focuses on electric machine analysis, design optimization, fault diagnosis with both physics modeling and machine learning techniques.

Chungwei Lin received his Ph.D. degree of Physics from Columbia University, New York, in 2008. He joined Mitsubishi Electric Research Laboratories (MERL) in 2015. He has applied quantum mechanics to model the magnetism, superconductivity, electronic structures observed in materials, particularly oxides. Since joining MERL, he has been working on photovoltaic, electroluminescent cooling, motor thermal modeling, and quantum technology.

Hiroshi Inoue received B.E.and M.E. degree from The University of Tokyo, Japan, in 2012 and 2014, respectively. He has been a researcher at Mitsubishi Electric Corporation since April 2014. His primary research focus is motor malfunction diagnosis technology. He is currently a member of the Mitsubishi Electric Advanced Technology R&D Center, Electromechanical Systems Department.

Makoto Kanemaru received B.E., M.E. and Ph.D. degree from Tokyo Institute of Technology, Japan, in 2006, 2008 and 2011, respectively. He has been a researcher at Mitsubishi Electric Corporation since April 2011. From 2019 to 2020, he was a visiting scholar at Walter H. Shorenstein Asia-Pacific Research Center, Stanford University, USA. His primary research focus is motor malfunction diagnosis technology. He is currently a group manager in Electromechanical Systems Department of the Mitsubishi Electric Advanced Technology R&D Center.